

Transfer-printed stacked nanomembrane lasers on silicon

Hongjun Yang^{1,3}, Deyin Zhao¹, Santhad Chuwongin¹, Jung-Hun Seo², Weiquan Yang¹, Yichen Shuai¹, Jesper Berggren⁴, Mattias Hammar⁴, Zhenqiang Ma^{2*} and Weidong Zhou^{1*}

The realization of silicon-based light sources has been the subject of a major research and development effort worldwide. Such sources may help make integrated photonic and electronic circuitry more cost-effective, with higher performance and greater energy efficiency. The hybrid approach, in which silicon is integrated with a III–V gain medium, is an attractive route in the development of silicon lasers because of its potential for high efficiency. Hybrid lasers with good performance have been reported that are fabricated by direct growth or direct wafer-bonding of the gain medium to silicon. Here, we report a membrane reflector surface-emitting laser on silicon that is based on multilayer semiconductor nanomembrane stacking and a stamp-assisted transfer-printing process. The optically pumped laser consists of a transferred III–V InGaAsP quantum-well heterostructure as the gain medium, which is sandwiched between two thin, single-layer silicon photonic-crystal Fano resonance membrane reflectors. We also demonstrate high-finesse single- or multiwavelength vertical laser cavities.

Since their invention 50 years ago, semiconductor lasers¹, mostly based on compound semiconductor heterostructures, have made a tremendous impact on modern science and technology, with widespread applications in areas such as communications, imaging, displays, medicine and optical physics. However, the realization of practical light sources on silicon substrates, the so-called ‘bread-and-butter’ material of the electronics industry, has proven to be a major barrier in the generation of silicon-based integrated photonics and electronics in large volumes and at low cost^{2–4}. Various approaches have been taken in the attempt to make light sources based on light emission from the silicon material itself, including the use of engineered silicon or germanium structures^{4,5} and stimulated Raman scattering in silicon^{6,7}. However, the lasers obtained by these means have extremely low efficiencies because of the inefficient light emission from silicon, which is an indirect-bandgap semiconductor material. Lasing with silicon has also been pursued based on the heterogeneous integration of silicon with compound semiconductor materials; in this case the emission originates from the use of efficient direct-bandgap (for example, group III–V) materials. Promising performances have been reported for these silicon-based lasers, which are fabricated by the direct growth of III–V materials on silicon^{8–10} or by bonding III–V wafers to silicon^{11–16}. However, challenges still remain for these hybrid approaches¹⁷. Direct (molecular) wafer bonding or wafer fusion has stringent bonding interface requirements, although these requirements can be relaxed by using an adhesive-assisted wafer-bonding technique¹³. Also, the direct growth of III–V materials on silicon is limited by lattice mismatches between the different material systems, as well as the incompatibility of different material growth conditions. Most on-silicon lasers reported to date are edge-emitting lasers, and for these, inherent challenges exist in forming cleaved mirror facets, in complementary metal-oxide-semiconductor (CMOS) compatible on-chip testing, and in forming large and dense laser arrays. In practical silicon photonics applications,

compact vertical-cavity surface-emitting lasers (VCSELs) are highly desirable, with compact mirrors such as very thin photonic-crystal mirrors (PCMs) being favoured over conventional thick distributed Bragg reflectors (DBRs)^{18–26}. The recent notable demonstration of silicon-based VCSELs made use of double one-dimensional PCMs and III–V/SiO₂ molecular bonding processes¹⁴, with a 2-inch III–V wafer being bonded to a SiO₂-coated 200 mm silicon-on-insulator (SOI) wafer, followed by an InP substrate removal process. The polarization-dependent one-dimensional PCM on top was formed on a deposited amorphous-silicon film using deep-ultraviolet lithography and reactive-ion etching. With this design, optically pumped room-temperature lasing with a low lasing threshold was reported in the 1,550 nm wavelength region.

Here, we report an optically pumped ultracompact silicon membrane reflector VCSEL (MR-VCSEL) that can be built easily using low-temperature membrane transfer printing and stacking fabrication processes^{27,28}. This new approach allows the facile fabrication of lasers on a full silicon wafer or any other low-cost or low-temperature substrates, without using wafer bonding. More importantly, the new processes enable the most efficient use of III–V materials in lasers without using multiple III–V wafers to cover the entire area of a large silicon wafer, with the additional advantage of recycling the III–V substrates²⁷. Furthermore, for single- or multiwavelength laser arrays, the new processes allow the arrays to be built in an arbitrarily distributed, dense or sparse fashion on a silicon substrate, based on the previously demonstrated feasibility²⁷.

Cavity design and fabrication

As shown schematically in Fig. 1a, the lasing cavity consists of a transferred III–V InGaAsP quantum well heterostructure active region, which is sandwiched between two single-layer silicon photonic-crystal Fano resonance membrane reflectors. These two membrane reflectors essentially replace the two multilayer quarter-wavelength DBRs that are commonly used in conventional

¹Department of Electrical Engineering, NanoFAB Center, University of Texas at Arlington, Texas 76019, USA, ²Department of Electrical and Computer Engineering, University of Wisconsin-Madison, Wisconsin 53706, USA, ³Semerane, Inc., 202 East Border Street, Suite 149, Arlington, Texas 76010, USA, ⁴KTH-Royal Institute of Technology, School of Information and Communication Technology, Electrum 229, 164 40 Kista, Sweden.

*e-mail: mazq@engr.wisc.edu; wzhou@uta.edu

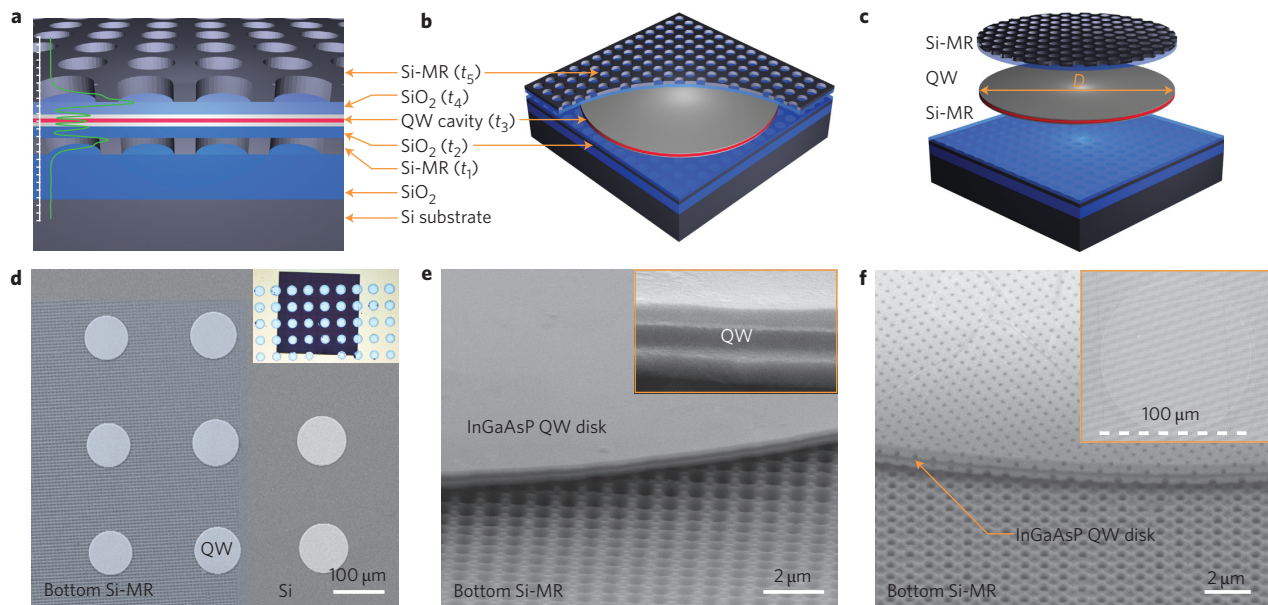


Figure 1 | MR-VCSEL on silicon. **a**, Schematic of a lasing cavity that consists of five layers (t_1 – t_5), with a total thickness of 1–2 wavelengths. An InGaAsP quantum well is sandwiched between two single-layer Si-MRs. Also shown is a simulated electrical field distribution in the cavity for a lasing mode at 1,527 nm, with a confinement factor of 6%. **b**, A cutout view of the complete MR-VCSEL. **c**, Illustration of the multilayer printing process for the formation of an MR-VCSEL (top Si-MR/quantum well/bottom Si-MR). The diameter of the active area is D . **d**, SEM image of InGaAsP quantum well disks/mesas transferred onto a bottom Si-MR. Inset: optical image, showing a central dark region representing the $1 \times 1 \text{ mm}^2$ bottom membrane reflector. **e**, Zoom-in view of one InGaAsP quantum well disk on the bottom Si-MR. Inset: quantum well heterostructure. **f**, SEM image of a complete MR-VCSEL, showing an InGaAsP quantum well disk sandwiched between top and bottom Si-MRs. Inset: SEM top view of an InGaAsP quantum well disk underneath a large top Si-MR layer.

VCSELs. The use of membrane reflectors allows the lasers to be built directly on silicon substrates but with much reduced laser dimensions (height), leading to a total near-infrared (NIR) membrane-reflector VCSEL cavity thickness of $<2 \mu\text{m}$ (for five layers, t_1 to t_5 , as defined in Fig. 1a). The unique laser features enable the creation of high-performance lasers on silicon, as well as a planar cavity structure that allows much simpler integration schemes with CMOS electronics. Also shown in Fig. 1a is the simulated optical E -field distribution profile for the designed lasing cavity mode at 1,527 nm. A confinement factor of 6% was obtained, which is similar to the values obtained from conventional DBR-based VCSELs²⁹. Such an ultrathin cavity has a much tighter field distribution than DBR-based VCSELs, with significantly reduced energy penetration depth and reduced cavity lengths³⁰. By further reducing the lateral cavity size to a few micrometres, there is the potential for such MR-VCSELs to have greatly reduced power consumption, improved power efficiency and higher modulation speed²⁹.

The multilayer Si-MR/quantum well/Si-MR MR-VCSEL cavity (Fig. 1b) was formed using semiconductor nanomembrane transfer printing and stacking processes²⁷. A polydimethylsiloxane (PDMS) stamp was developed and optimized for ultrathin and large hole-to-neck ratio photonic-crystal nanomembrane pick-up and transfer from a source substrate to a foreign destination substrate²⁴. Elsewhere, this PDMS transfer printing has been applied to a wide range of material systems, with demonstrations in various electronic, optoelectronic and photonic devices^{27,28,31–35}.

Here, we illustrate the first multilayer *stacked* laser cavity on silicon, making use of a two-step nanomembrane transfer printing process (Fig. 1c). The high-quality active region of the laser cavity, which consists of an undoped strain-compensated InGaAsP quantum-well active region³⁶ and doped p- and n-InP cladding layers, was obtained by being released as a membrane from a source InP substrate. A sacrificial InGaAs layer was first grown on an InP substrate, followed by growth of the InGaAsP quantum-well active region. The InGaAsP quantum-well active region was then

released from the InP substrate using a selective wet-etching process. The metal organic chemical vapour deposition (MOCVD)-grown quantum-well λ -cavity consists of eight strain-compensated $\text{In}_{0.76}\text{Ga}_{0.24}\text{As}_{0.83}\text{P}_{0.17}/\text{In}_{0.485}\text{Ga}_{0.515}\text{As}_{0.83}\text{P}_{0.17}$ quantum wells with a centre emission wavelength of $\sim 1,527 \text{ nm}$ at room temperature³⁶. To form a complete MR-VCSEL cavity, the InGaAsP quantum-well heterostructure was first released and transferred onto the lower Si-MR, followed by a further PDMS transfer of an upper Si-MR onto the top of the transferred InGaAsP quantum-well nanomembrane. As reported here, despite stringent requirements regarding mirror reflectivity (R) and for high cavity quality factors (Q), multilayer high-quality PDMS transfer printing is feasible for the construction of MR-VCSEL cavities with high finesse. Further information on the fabrication process can be found in Supplementary Section I, Fig. S1.

Figure 1d presents a scanning electron micrograph (SEM) image of InGaAsP quantum-well disks that have been transferred onto the bottom Si-MR. Six quantum well disks have been transferred onto the patterned Si-MR region, while two disks are located on the unpatterned silicon region. The disks (the active area of the MR-VCSELs) have an average diameter D of $100 \mu\text{m}$. The inset of Fig. 1d shows a top-view micrograph of the fabricated device, with the quantum well disks transferred onto the bottom Si-MR (dark coloured square). A magnified view of an InGaAsP quantum well disk on the bottom Si-MR is shown in Fig. 1e, with a zoom-in view of the InGaAsP quantum well heterostructure λ -cavity shown in the inset. A complete MR-VCSEL structure is shown in Fig. 1f, with both top and bottom Si-MRs visible, and the inset to Fig. 1f shows a single quantum well disk under the top Si-MR layer.

The design and measurement results for the top and bottom membrane reflectors are summarized in Fig. 2. As an alternative to conventional multilayer DBRs, other structures that can be used as ultracompact broadband reflectors hold great promise in a wide range of device applications, including single-layer

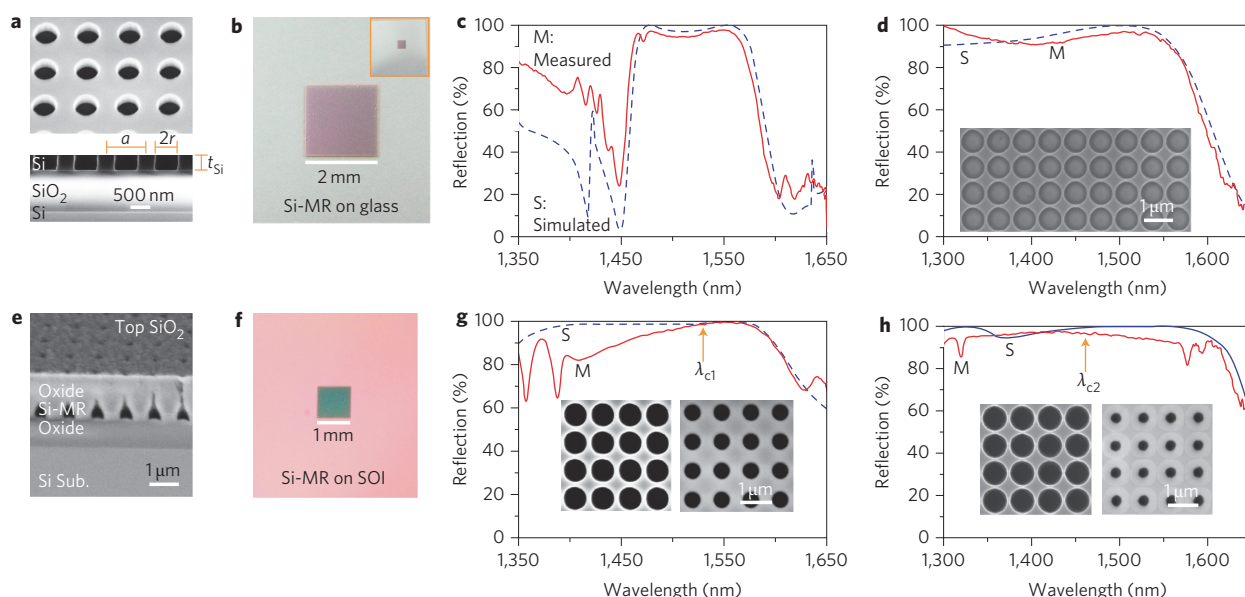


Figure 2 | Top and bottom membrane reflector performances. Top row shows results for top membrane reflectors. Bottom row show results for bottom membrane reflectors. **a**, SEM images (top and cross-sectional views) of a fabricated Si-MR on SOI. The key design parameters are lattice constant a , air hole radius r and membrane reflector thickness t_{Si} . **b**, Micrograph image of a fabricated top Si-MR transferred onto a glass substrate. **c,d**, Simulated (S) and measured (M) reflection spectra for the top Si-MR on glass designed for the 1,550 nm spectral band (**c**, RT design: $a = 980$ nm, $r/a = 0.275$) and for the 1,450 nm spectral band (**d**, LT design: $a = 860$ nm, $r/a = 0.46$), with the inset to **d** showing a zoom-in SEM image. **e**, SEM image of a fabricated bottom Si-MR on SOI, with a SiO_2 low-index buffer layer (t_2) deposited on top. **f**, Micrograph image of a fabricated bottom Si-MR on an SOI substrate. **g,h**, Simulated (S) and measured (M) reflection spectra for the bottom Si-MR (with a SiO_2 t_2 layer) designed for 1,550 nm (**g**, RT design: $a = 880$ nm, $r/a = 0.45$) and 1,450 nm (**h**, LT design: $a = 880$ nm, $r/a = 0.47$) spectral bands. Insets: SEM top-view images of the bottom Si-MR before and after SiO_2 (t_2) layer deposition.

high-index-contrast gratings (HCGs), guided-mode resonance (GMR) gratings and two-dimensional photonic-crystal slab (2D PCS) Fano resonance structures^{18–26}. The arrangement shown in Fig. 2a makes use of a square lattice air hole PCS structure on SOI for the membrane reflectors. Its key design parameters are lattice constant a , air hole radius r and Si-MR thickness t_{Si} . For all the membrane reflectors reported here, $t_{\text{Si}} = 340$ nm. We used two designs/configurations to obtain MR-VCSEL cavities with different cavity resonances that operated at room temperature (RT design) and low temperature (LT design), respectively, as shown in Fig. 2b–h. For the top membrane reflector used in the lasers reported here, we first transferred the fabricated Si-MR to a transparent glass substrate, then transferred the glass substrate holding the Si-MR onto the top of the InGaAsP quantum well disks. Figure 2b shows a micrograph of the transferred Si-MR on glass. The measured and simulated reflection spectra are shown in Fig. 2c,d for the top Si-MRs with the spectral bands centred around 1,550 nm and 1,450 nm to match the InGaAsP quantum well emission wavelength at room temperature (Fig. 2c) and low temperature (Fig. 2d). The bottom Si-MR was directly fabricated on an SOI substrate, followed by deposition of a thin SiO_2 film on top, with the SiO_2 layer thickness varying in the range $t_2 \approx 350$ –400 nm depending on the desired cavity resonance spectral location. Note that other low-index materials such as Al_2O_3 or diamond can also be used to achieve improved thermal conductivity and power dissipation handling. A cross-sectional SEM image is provided in Fig. 2e, showing the high-index patterned Si-MR layer embedded between the top and bottom low-index oxide layers. A micrograph is also shown in Fig. 2f of a fabricated 1×1 mm² bottom Si-MR on the SOI substrate. Figure 2g,h presents the measured and simulated reflection spectra for bottom Si-MRs with top SiO_2 thicknesses t_2 of 365 nm and 383 nm in an attempt to match the spectral band centred around 1,550 nm (RT design) and 1,450 nm (LT design), respectively. SEM images without and with the top SiO_2 layer are also shown in the insets of Fig. 2g,h.

Note that, because of the different vertical index profiles of the top and bottom MRs, different sets of design parameters (a , r) are used so that the reflection spectral band covers the designed wavelengths. All the reflectors designed and demonstrated here have peak reflection values that are $>99\%$, with different high reflection bands.

The design of the lasing cavity was carried out carefully to allow us to examine the lasing cavity properties (see Supplementary Section II, Fig. S2 for more details). Great care was taken to design and separate the competing lasing cavity modes from the waveguide modes within the InGaAsP quantum well λ -cavity region. As a result of the drastically different phase differences and different reflection mechanisms, the cavity resonance modes and the field distribution profiles are quite different from those of lasing cavities formed using two conventional DBRs³⁰. Despite the relatively large field concentration in the high-index Si-MR layer, the lasing mode field confinement factor (that is, the overlap between the standing wave field distribution and the quantum well active region) is 6% for MR-VCSELs, which is comparable to that of conventional DBR-based VCSELs. Such a high confinement factor may be a result of the much reduced lasing cavity length and stronger cavity confinement, considering the reduced field penetration depths and membrane reflector large-index contrasts.

Device characterization

Two types of MR-VCSEL devices were fabricated for separate LT and RT operations. Shown in Figs 3 and 4 are the measured characteristics for the MR-VCSEL based on the LT and RT designs (shown in Fig. 2), respectively. Note that the total vertical cavity thickness is only 2.4 μm . All tests were carried out using a monochromator-based optically pumped micro-photoluminescence (μPL) set-up by placing the sample inside a cryostat while varying the temperature from 10 K to 300 K. A continuous-wave (c.w.) green laser with an emission wavelength of 532 nm was used as the pump source, and a chopper and lock-in amplifier were used for data

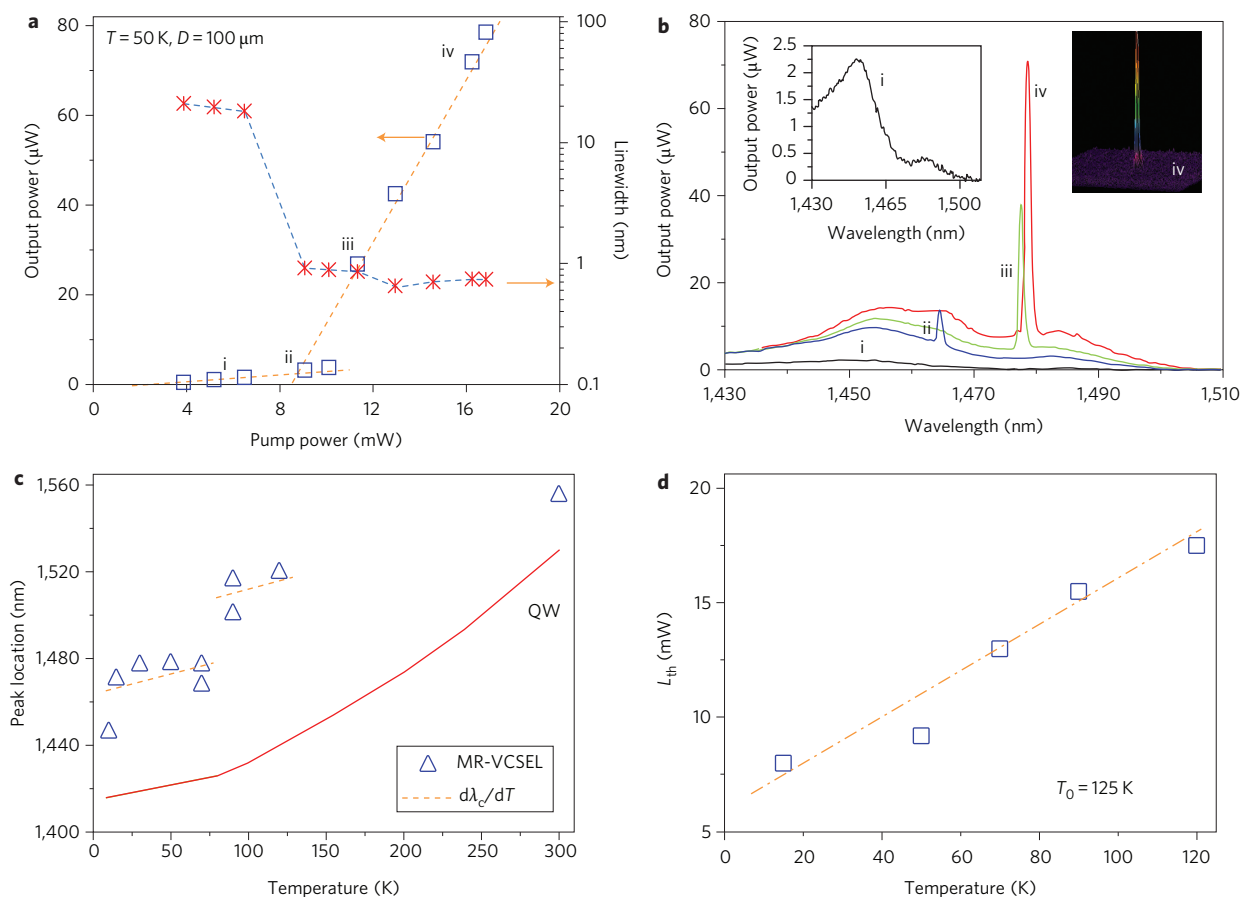


Figure 3 | Low-temperature MR-VCSEL performances. **a**, Lasing power and linewidth versus input power. **b**, Measured spectral outputs of the MR-VCSEL at four pump power levels: below (i), at (ii) and above (iii, iv) threshold. Inset (left): spontaneous emission spectrum below threshold. Inset (right): far-field image above threshold. **c**, Measured temperature-dependent lasing peaks, as well as calculated cavity resonance shift ($d\lambda_c/dT$). Also shown is the measured as-grown quantum well emission spectral shift with temperature. **d**, Measured lasing threshold power for different temperatures, with a characteristic temperature T_0 of 125 K.

acquisition. Spectrally resolved lasing output was detected with a thermoelectric cooled InGaAs detector.

The L–L plot (light output for different input light pump powers) and the corresponding spectral linewidths are shown in Fig. 3a for a LT design of MR-VCSEL device. The threshold pump power is $\sim 8\text{ mW}$, or 0.32 kW cm^{-2} . A more detailed discussion about output power can be found in Supplementary Section III. The measured spectral linewidths reduce from 30 nm below threshold to 0.6–0.8 nm above threshold. The measured spectral outputs are shown in Fig. 3b for pump power below, at and above threshold (corresponding to the similarly labelled points in the L–L plot of Fig. 3a). For better visibility, the spectrum below threshold is magnified and shown in the left inset of Fig. 3b. The lasing spectral linewidth is $\sim 8\text{ }\text{\AA}$, which is essentially limited by the measurement set-up. Also shown in Fig. 3b (right inset) is a measured far-field image for the MR-VCSEL biased above threshold (data point (iv) on the L–L curve), with collimated circular single-mode output.

The relative peak location shift shown in Fig. 3b for bias levels (ii) and (iii, iv) is predominantly related to mode hopping and temperature rise inside the active region at higher pump power levels. The peak shift is also evident in Fig. 3c, where the lasing peak locations shift towards longer wavelengths with increasing temperature at a rate of $d\lambda_c/dT$, close to the simulated 0.088 nm K^{-1} . Mode hopping is evident below and above an operation temperature of 80 K. The MR-VCSEL device was characterized at different temperatures up to 120 K, which was mainly limited by the membrane

reflector bandwidth. For reference, also shown in Fig. 3c is the temperature-dependent emission peak measured for an as-grown quantum well sample. The quantum well emission peak has a redshift at a rate of 0.43 nm K^{-1} as the temperature rises. For this set of LT MR-VCSEL samples, the measured temperature-dependent lasing threshold is shown in Fig. 3d, where the extracted characteristic temperature T_0 is 125 K.

A different set of MR-VCSELs was also fabricated for quasi-c.w. mode lasing at room temperature, with both top and bottom membrane reflectors centred at the 1,550 nm band (RT design). The optical characteristics are shown in Fig. 4a. The pump threshold is 18 mW, which is very similar to the low-temperature threshold at 120 K (Fig. 3d). The lasing spectral linewidth is $\sim 0.9\text{ nm}$. Currently this MR-VCSEL thermal performance is limited by the use of a low-index SiO_2 layer, which has very poor thermal conductivity.

Multiwavelength operation

Multiwavelength MR-VCSEL arrays can also be realized on a single silicon substrate by simply releasing and transfer-printing different III–V structures and photonic-crystal membrane reflectors with different lattice parameters, thereby demonstrating the superior flexibility and practicality of this new laser fabrication approach. Figure 4b demonstrates different lasing wavelengths based on membrane reflectors made to the LT and RT designs. For the LT design of cavity, lasing wavelengths of 1,448 nm (at 10 K), 1,478 nm (at 50 K) and 1,520 nm (at 120 K) were obtained at different temperatures. For the RT design of cavity, a lasing wavelength of 1,556 nm was

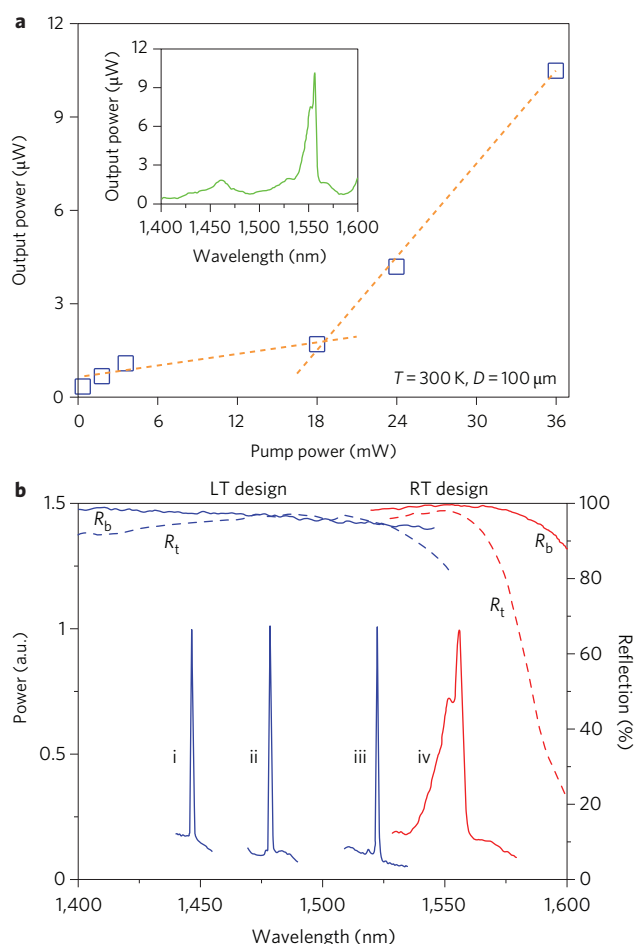


Figure 4 | RT design of MR-VCSELs and multispectral lasing. **a**, Laser L-L curve at room temperature for the RT design of MR-VCSEL device. Inset: measured spectral output above threshold at a pump power of 36 mW. **b**, Measured MR-VCSEL spectral outputs at different temperatures for both LT and RT designs: (i) $T = 10$ K; (ii) $T = 50$ K; (iii) $T = 120$ K; (iv) $T = 300$ K. Portions of measured top (R_t , dash lines) and bottom (R_b , solid lines) reflection spectra are also shown for both LT and RT designs.

obtained. These lasing wavelengths match well with the cavity resonances based on the different designs. Although the current laser demonstration was made on a small substrate, there are no intrinsic limitations to scaling up this transfer-printing and stacking process to full wafer scale. Indeed, full wafer upscaling can be realized simply by repeating the transfer-printing procedure in a manner similar to that used in stepper lithography. Practical issues associated with upscaling include maintaining the flatness of large silicon nanomembrane mirrors, forming large-area nanoscale patterning for mirrors at low cost, and minimizing PDMS stamp-induced stress during mirror transfer. All these issues are readily resolvable with existing solutions. Based on the optical pump results, it is feasible to create electrically injected MR-VCSELs by incorporating intracavity electrodes into the InGaAsP quantum well λ -cavity region, similar to the configuration commonly adopted in conventional VCSELs, where both p- and n-contacts will be formed directly on the InGaAsP quantum well p-i-n active layer. Construction of such electrically injected lasers is currently under way.

Conclusion

In summary, we have demonstrated an ultrathin DBR-free MR-VCSEL on silicon, based on transfer-printed InGaAsP

quantum well cavities sandwiched between a bottom Si-MR and a top transfer-printed Si-MR. The entire lasing cavity was built with low-temperature processes on CMOS-compatible silicon substrates. In contrast to conventional DBR-based VCSELs, which may be bonded/transferred onto silicon substrates after completing their fabrication on III-V substrates, the multilayer membrane transfer-printing process offers a very simple and flexible approach to large-scale photonic integration. It differs also from direct wafer-fusing/bonding approaches, in that the transfer-printed multilayer membranes can be used with different types of interface control and engineering measures, allowing better thermal mismatch tolerance between dissimilar materials. With this demonstrated approach to lasers on silicon, different material systems can be further integrated, unlocking the constraints regarding lattice mismatch and thermal mismatch and opening the door to a wide range of applications in optoelectronic and photonic devices, and integrated systems thereof.

The ultracompact high-finesse Fabry-Perot cavity, based on two parallel single-layer Si-MRs, offers a simple solution to VCSELs on silicon and on any other substrates. The approach also renders wavelength scalability and tunability. Electrical injection is also feasible with the incorporation of intracavity contacts. Notably, such MR-VCSEL devices can be further integrated with different functional photonic nanomembrane layers for modulation, beam focusing and routing, and three-dimensional photonic/electronic integration. Finally, the MR-VCSEL devices can be built and transferred onto any other rigid glass or flexible plastic substrate, making them even more attractive for applications in consumer electronics, biophotonics, and so on.

Received 8 March 2012; accepted 27 May 2012;
published online 22 July 2012

References

- Maiman, T. H. Stimulated optical radiation in ruby. *Nature* **187**, 493–494 (1960).
- Miller, D. Device requirements for optical interconnects to silicon chips. *Proc. IEEE* **97**, 1166–1185 (2009).
- Soref, R. A. The past, present, and future of silicon photonics. *IEEE J. Sel. Top. Quantum Electron.* **12**, 1678–1687 (2006).
- Pavesi, L. Will silicon be the photonic material for the third millennium? *J. Phys. Condens. Matter* **15**, R1169–R1196 (2003).
- Liu, J. F., Sun, X. C., Camacho-Aguilera, R., Kimerling, L. C. & Michel, J. Ge-on-Si laser operating at room temperature. *Opt. Lett.* **35**, 679–681 (2010).
- Boyras, O. & Jalali, B. Demonstration of a silicon Raman laser. *Opt. Express* **12**, 5269–5273 (2004).
- Rong, H., Liu, A. & Paniccia, M. An all-silicon Raman laser. *Nature* **433**, 292–294 (2005).
- Chen, R. et al. Nanolasers grown on silicon. *Nature Photon.* **5**, 170–175 (2011).
- Mi, Z., Bhattacharya, P., Yang, J. & Pipe, K. P. Room-temperature self-organized $\text{In}_{0.5}\text{Ga}_{0.5}\text{As}$ quantum dot laser on silicon. *Electron. Lett.* **41**, 742–744 (2005).
- Balakrishnan, G. et al. Room-temperature optically pumped (Al) GaSb vertical-cavity surface-emitting laser monolithically grown on an Si(100) substrate. *IEEE J. Sel. Top. Quantum Electron.* **12**, 1636–1641 (2006).
- Bowers, J. E. et al. Design and fabrication of optically pumped hybrid silicon-AlGaInAs evanescent lasers. *IEEE J. Sel. Top. Quantum Electron.* **12**, 1657–1663 (2006).
- Van Campenhout, J. et al. Electrically pumped InP-based microdisk lasers integrated with a nanophotonic silicon-on-insulator waveguide circuit. *Opt. Express* **15**, 6744–6749 (2007).
- Stankovic, S. et al. 1310 nm hybrid III-V/Si Fabry-Perot laser based on adhesive bonding. *IEEE Photon. Technol. Lett.* **23**, 1781–1783 (2011).
- Sciancalepore, C. in *8th IEEE International Conference on Group IV Photonics (GFP)* 205–207 (IEEE, 2011).
- Bakir, B. B. et al. Surface-emitting microlaser combining two-dimensional photonic crystal membrane and vertical Bragg mirror. *Appl. Phys. Lett.* **88**, 081113 (2006).
- Roelkens, G. et al. III-V/silicon photonics for on-chip and intra-chip optical interconnects. *Laser Photon. Rev.* **4**, 751–779 (2010).
- Moutanabbir, O. & Gösele, U. Heterogeneous integration of compound semiconductors. *Annu. Rev. Mater. Res.* **40**, 469–500 (2010).
- Fan, S. & Joannopoulos, J. D. Analysis of guided resonances in photonic crystal slabs. *Phys. Rev. B* **65**, 235112 (2002).

19. Lousse, V. *et al.* Angular and polarization properties of a photonic crystal slab mirror. *Opt. Express* **12**, 1575–1582 (2004).
20. Mateus, C. F. R., Huang, M. C. Y., Chen, L., Chang-Hasnain, C. J. & Suzuki, Y. Broadband mirror (1.12–1.62 μm) using single-layer sub-wavelength grating. *IEEE Photon. Technol. Lett.* **16**, 1676–1678 (2004).
21. Boutami, S. *et al.* Broadband and compact 2-D photonic crystal reflectors with controllable polarization dependence. *IEEE Photon. Technol. Lett.* **18**, 835–837 (2006).
22. Magnusson, R. & Shokoooh-Saremi, M. Physical basis for wideband resonant reflectors. *Opt. Express* **16**, 3456–3462 (2008).
23. Yang, H. *et al.* Resonance control of membrane reflectors with effective index engineering. *Appl. Phys. Lett.* **95**, 023110 (2009).
24. Yang, H. *et al.* Broadband membrane reflectors on glass. *IEEE Photon. Technol. Lett.* **24**, 476–478 (2012).
25. Huang, M. C. Y., Zhou, Y. & Chang-Hasnain, C. J. A surface-emitting laser incorporating a high-index-contrast subwavelength grating. *Nature Photon.* **1**, 119–122 (2007).
26. Boutami, S., Bakir, B., Regreny, P., Leclercq, J. & Viktorovitch, P. Compact 1.55 μm room-temperature optically pumped VCSEL using photonic crystal mirror. *Electron. Lett.* **43**, 282–283 (2007).
27. Meitl, M. A. *et al.* Transfer printing by kinetic control of adhesion to an elastomeric stamp. *Nature Mater.* **5**, 33–38 (2006).
28. Sun, L., Qin, G., Celler, G. K., Zhou, W. & Ma, Z. 12-GHz thin-film transistors with transferrable silicon nanomembranes for high-performance massive flexible electronics (cover story). *Small* **6**, 2553–2557 (2010).
29. Wilmsen, C. W., Temkin, H. & Coldren, L. A. *Vertical-Cavity Surface-Emitting Lasers: Design, Fabrication, Characterization, and Applications* Vol. **24** (Cambridge Univ. Press, 2001).
30. Zhao, D., Ma, Z. & Zhou, W. Field penetrations in photonic crystal Fano reflectors. *Opt. Express* **18**, 14152–14158 (2010).
31. Yuan, H. C., Ma, Z., Roberts, M. M., Savage, D. E. & Lagally, M. G. High-speed strained-single-crystal-silicon thin-film transistors on flexible polymers. *J. Appl. Phys.* **100**, 013708 (2006).
32. Zhou, W. *et al.* Flexible photonic-crystal Fano filters based on transferred semiconductor nanomembranes. *J. Phys. D* **42**, 234007 (2009).
33. Rogers, J. A., Someya, T. & Huang, Y. Materials and mechanics for stretchable electronics. *Science* **327**, 1603–1607 (2010).
34. Rogers, J. A., Lagally, M. G. & Nuzzo, R. G. Synthesis, assembly and applications of semiconductor nanomembranes. *Nature* **477**, 45–53 (2011).
35. Zhang, K., Seo, J. H., Zhou, W. & Ma, Z. Fast flexible electronics using transferrable silicon nanomembranes (topical review). *J. Phys. D* **45**, 143001 (2012).
36. Rapp, S. *et al.* All-epitaxial single-fused 1.55 μm vertical cavity laser based on an InP Bragg reflector. *Jpn J. Appl. Phys* **38**, 1261–1264 (1999).

Acknowledgements

This work was supported by US AFOSR STTR programmes FA9550-09-C-0200 and FA9550-11-C-0026 and by US ARO (W911NF-09-1-0505). The silicon nanomembrane work was partially supported by an AFOSR MURI programme (FA9550-08-1-0337), and the initial membrane reflector work was supported by DARPA YFA (HR80011-08-1-0058). The AFOSR programme manager is G. Pomrenke and the ARO programme manager is M. Gerhold. The authors also acknowledge help and support from R. Soref, Z. Qiang, S. Fan, J. A. Rogers, S. Wang, R. Li, T. Saha, H. Mi and G. Gui on this project.

Author contributions

H.Y., S.C., Y.S., Z.M. and W.Z. contributed to device fabrication. D.Z., Z.M. and W.Z. contributed to device design. W.Y., J.S., S.C., Z.M. and W.Z. contributed to nanomembrane transfer printing. H.Y., D.Z., S.C., Z.M. and W.Z. contributed to device characterization. J.B. and M.H. contributed to InGaAsP quantum well epitaxial growth. Z.M. and W.Z. guided the project. H.Y., D.Z., Z.M. and W.Z. wrote the paper.

Additional information

The authors declare no competing financial interests. Supplementary information accompanies this paper at www.nature.com/naturephotonics. Reprints and permission information is available online at <http://www.nature.com/reprints>. Correspondence and requests for materials should be addressed to Z.M. and W.Z.